

IN-ORBIT PERFORMANCE OF THE CONSTELLATION OF CYGNSS HURRICANE SATELLITES

CHRISTOPHER RUF, SHAKEEL ASHARAF, RAJESWARI BALASUBRAMANIAM, SCOTT GLEASON, TIMOTHY LANG, DARREN MCKAGUE, DORINA TWIGG, AND DUANE WALISER

The retrieval of ocean surface wind speed from the recently launched CYGNSS constellation of satellites is characterized with respect to uncertainty, dynamic range, spatial resolution, spatial and temporal sampling, and data latency.

The Cyclone Global Navigation Satellite System (CYGNSS) is a NASA spaceborne mission consisting of eight spacecraft in a common circular low Earth orbit at 35° inclination and 520-km altitude. The spacecraft carry radar receivers tuned

to measure global positioning system (GPS) signals scattered from the ocean surface in the forward (specular) direction. This remote sensing method is commonly referred to as Global Navigation Satellite System reflectometry (GNSS-R). The strength of the scattered signals is affected by surface roughness and near-surface wind speed. CYGNSS estimates the wind speed from its radar measurements (Clarizia and Ruf 2016a). Winds are measured continuously over the ocean in all weather conditions, although the mission objectives are focused on measurements made in and near the inner core of tropical cyclones (Ruf et al. 2016).

The CYGNSS constellation was successfully launched on 15 December 2016. Following an initial engineering commissioning phase, science measurements began in March 2017 and have continued uninterrupted since then. Early science activities focused on development of the wind speed retrieval algorithm and validation of the data products. Nonprovisional public release of those products by the NASA PO.DAAC began in November 2017 at the end of the 2017 Atlantic hurricane season (PO.DAAC 2018). More recently, science activities have focused on refinements to the data products (Gleason et al. 2018; Ruf and

AFFILIATIONS: RUF, BALASUBRAMANIAM, MCKAGUE, AND TWIGG—University of Michigan, Ann Arbor, Michigan; ASHARAF—Joint Institute for Regional Earth System Science and Engineering, University of California, Los Angeles, Los Angeles, and Jet Propulsion Laboratory, California Institute of Technology, Pasadena, California; GLEASON—University Corporation for Atmospheric Research, Boulder, Colorado; LANG—NASA Marshall Space Flight Center, Huntsville, Alabama; WALISER—Jet Propulsion Laboratory, California Institute of Technology, Pasadena, California

CORRESPONDING AUTHOR: Prof. Christopher Ruf, cruf@umich.edu

The abstract for this article can be found in this issue, following the table of contents.

DOI:10.1175/BAMS-D-18-0337.1

A supplement to this article is available online (10.1175/BAMS-D-18-0337.2)

In final form 7 June 2019

©2019 American Meteorological Society

For information regarding reuse of this content and general copyright information, consult the [AMS Copyright Policy](#).

Balasubramaniam 2018), on assimilation of the wind speed data into numerical prediction models (Pu et al. 2018; Zhang et al. 2017), and on the use of surface scattering measurements made over land for soil moisture and flooding applications (Chew et al. 2018; Jensen et al. 2018; Kim and Lakshmi 2018; Ruf et al. 2018a).

Every NASA science mission has level 1 mission science requirements (L1 requirements). Prior to launch, they are used as guiding principles to aid in design of the mission architecture and of the satellites and science payloads. Once on orbit, they continue to aid in decision-making about the mission execution. It is also useful to consider the requirements as metrics for mission success writ large. To that end, a quantitative assessment is presented here of CYGNSS performance with respect to each of its L1 requirements. More than simply an answer to the question “Is the CYGNSS mission a success?” the assessment provides a detailed characterization of the quantity and quality of science data products produced by the mission. It can serve as a guide for potential science data users who are not familiar with the details of the mission or its measurement technique, to inform them of its capabilities and hopefully encourage them to consider using the data in their own science investigations.

The CYGNSS L1 requirements fall into several categories: spatial and temporal sampling properties; dynamic range and uncertainty of wind speed measurements; and data validation and support for operational data users. The requirements are itemized in Table 1. The table lists both baseline and, where different, threshold requirements. Baseline requirements stipulate the target level of performance used to inform mission design decisions. Threshold requirements define mission success criteria.

CYGNSS performance is assessed in the following section relative to each of the requirements in Table 1.

In some cases, the assessment builds on previously published analyses of mission performance, updating them using more complete data records and more recent versions of the science data products. In other cases, new analyses are developed and their results presented.

REQUIREMENTS ASSESSMENT. *Wind speed dynamic range.* Both GNSS-R and conventional wind scatterometer sensors estimate wind speed indirectly from measurements of the radar cross section (RCS) of the ocean surface. The RCS is, in turn, determined by ocean surface roughness. In the case of conventional scatterometers, the radar receives the signal scattered back in the direction of its transmitter. This backscatter geometry results in the RCS being largely determined by the portion of the surface roughness spectrum near the Bragg resonant wavelength of the transmitted signal. In the case of scatterometers operating at C or X band, that wavelength is of order 2–10 cm. As a result, scatterometers are sensitive to the smaller capillary waves that tend to be strongly coupled to the local wind speed (Ulaby and Long 2014). GNSS-R measurements, on the other hand, are made with a forward (specular) scattering geometry for which Bragg resonance does not occur. As a result, its RCS measurements are sensitive to a broader range of the roughness spectrum that includes both capillary waves and longer swell (Zavorotny and Voronovich 2000). In an ideal fully developed sea state, with infinite fetch length and sea age, the energy introduced to the surface by local wind forcing has sufficient time and distance to cascade from short (capillary) to long (swell) waves, and the broad roughness spectrum sensed by a GNSS-R instrument is strongly coupled to the local wind speed. In young seas with limited fetch, the sea state

TABLE 1. CYGNSS level 1 mission science requirements.

No.	Requirement	Baseline	Threshold
1	Wind speed dynamic range at 5 km × 5 km resolution	3–70 m s ⁻¹	3–40 m s ⁻¹
2	Operation in presence of rain	Yes	Same as baseline
3a	Retrieval uncertainty for winds > 20 m s ⁻¹	10%	Same as baseline
3b	Retrieval uncertainty for winds < 20 m s ⁻¹	2 m s ⁻¹	Same as baseline
3c	Spatial resolution	25 km × 25 km or better	50 km × 50 km or better
4a	100% duty cycle during science operations	Yes	Same as baseline
4b	Mean temporal resolution	<12 h	Same as baseline
4c	Spatial sampling coverage of cyclone historical tracks in 24 h	70%	50%
5	Calibrate and validate CYGNSS data in individual wind speed bins above and below 20 m s ⁻¹	Yes	Same as baseline
6	Support operational hurricane forecast community	Yes	Same as baseline

is underdeveloped and only a portion of the roughness spectrum is a direct response to the local wind. In practice, the time required for the portion of the roughness spectrum sensed by a GNSS-R instrument to respond to changes in wind speed is estimated to be 0.4–1.8 h, depending on wind speed, fetch length, and atmospheric stability (Chen et al. 2016). As a result, in most open-ocean conditions in which the winds have been blowing steadily for 1–2 h, the sea state can be considered effectively fully developed for purposes of GNSS-R measurements. An important exception to this, which is addressed below, is the conditions in and near a tropical cyclone, where both the speed and direction of the wind can change more rapidly. One other important distinction between GNSS-R and conventional scatterometer measurements of the ocean lies in their relative sensitivity to wind direction. The RCS measured by a scatterometer is strongly dependent on wind direction and both the speed and direction can be determined given observations at multiple azimuthal angles. GNSS-R measurements, on the other hand, have a much weaker dependence on wind direction and only one azimuthal look angle. As a result, direction is not retrieved.

The near-surface wind speed estimated by CYGNSS is referenced to a height of 10 m. All wind speed requirements are with respect to this value, referred to as u_{10} . Two wind speed estimates are produced for each measurement. One is the fully developed seas (FDS) estimate, which is appropriate to use in most conditions. The other is the young seas/limited fetch (YSLF) estimate, which is used near the inner core of tropical cyclones (TCs) when the long-wave portion of the sea state has not responded fully to the local surface winds. Using a single YSLF characterization for all conditions in and near a TC is a simplifying approximation. For example, fetch length can vary by quadrant, depending on the relative orientation of the cyclonic rotation and the direction of translation of a storm. The use of a single YSLF assumption effectively averages across the range of departures from a fully developed state that are experienced in different quadrants of a TC. Incorporation of a more representative characterization of the sea state within a TC into the CYGNSS wind speed retrieval algorithm is an area of active research that is expected to improve wind speed retrieval performance by, for example, reducing quadrant-dependent errors.

The wind speed dynamic range requirement has a lower bound of 3 m s^{-1} for both baseline and threshold cases. The upper bound is 40 m s^{-1} for the threshold requirement and increases to 70 m s^{-1} for the baseline

requirement. In both cases, the relevant wind speed is a spatially averaged value over a $5 \text{ km} \times 5 \text{ km}$ area. This definition is intended to support direct comparisons between CYGNSS and measurements by the stepped frequency microwave radiometer (SFMR) on the NOAA P-3 “hurricane hunter” aircraft, which measure u_{10} in the inner core of hurricanes during eyewall penetration flights by the aircraft. SFMR measurements have a $\sim 5\text{-km}$ spatial resolution when flying at typical altitude (Uhlhorn et al. 2017). For direct comparisons between CYGNSS and SFMR, the SFMR measurements are averaged for a time corresponding to forward motion of the P-3 aircraft by 20 km, producing a $\sim 5 \text{ km} \times 25 \text{ km}$ effective footprint. The CYGNSS effective footprint size is $\sim 25 \text{ km} \times 25 \text{ km}$.

Dynamic range can be determined in two ways: empirically, through direct comparisons with independent, coincident measurements of wind speed; and by analysis, through extrapolation of the demonstrated performance to higher wind speeds by making assumptions about the sensitivity of the measurements at those higher wind speeds. The empirical approach is more direct and is preferred, in particular because it does not require assumptions about measurement sensitivity above the demonstrated dynamic range. For this reason, we use the empirical approach over the range of wind speeds for which independent, coincident measurements are available. The matchup datasets used to assess the uncertainty in CYGNSS wind speed measurements are described in the “Wind speed retrieval uncertainty $> 20 \text{ m s}^{-1}$ ” and “Wind speed retrieval uncertainty $< 20 \text{ m s}^{-1}$ ” sections below. Over the range $1\text{--}20 \text{ m s}^{-1}$, the assessment uses matchups with the Global Data Assimilation System (GDAS) numerical weather prediction model and with several buoy networks. Comparisons were also made with other NWP wind speed products, in addition to GDAS (e.g., ECMWF, MERRA-2). The matchup statistics are in each case very similar and are not included for brevity. Above 20 m s^{-1} , the assessment uses matchups with SFMR during hurricane eyewall penetrations that were coincident with CYGNSS overpasses. The range of wind speeds in the SFMR matchups covers $20\text{--}54 \text{ m s}^{-1}$. Direct empirical determination of the CYGNSS dynamic range thus covers wind speeds of $1\text{--}54 \text{ m s}^{-1}$.

Operation in the presence of rain. Due to the well-known scattering properties of microwave signals, it is expected that L-band measurements by CYGNSS should not be as sensitive to rain as measurements made at Ku band and C band (Marzano et al. 2000; Weissman et al. 2002; Tournadre and Quilfen 2003;

Milliff et al. 2004; Weissman and Bourassa 2008; Ruf et al. 2016; Meissner et al. 2017). Indeed, the stronger rain impacts at higher frequencies than L band have been exploited to make dual retrievals of both wind and rain by Ku- (Draper and Long 2004a,b; Nielsen and Long 2009; Owen and Long 2011) and C-band (Nie and Long 2007, 2008) wind scatterometers.

Following this logic, the ability of the CYGNSS mission to operate successfully in the presence of rain is demonstrated by comparing CYGNSS wind speed estimates to buoy-measured winds in precipitating conditions. For this analysis, we use the CYGNSS FDS wind speed estimates. While FDS winds are not expected to be accurate within TCs, the frequency and spatial coverage of major storms are so small at individual buoys that including these observations should not have a significant impact on results. Thus, no filtering for TCs was done in the dataset.

For 18 March 2017–23 August 2018, the Prediction and Research Moored Array in the Tropical Atlantic (PIRATA; Bourles et al. 2008), Research Moored Array for African–Asian–Australian Monsoon Analysis and Prediction (RAMA; McPhaden et al. 2009), and Tropical Atmosphere Ocean (TAO; McPhaden et al. 1998)/Triangle Trans-Ocean Buoy Network (TRITON) buoy datasets were matched to v2.1 CYGNSS winds in the following manner. All satellite observations are considered within 25 km and 0.5 h of buoy locations and times that featured hourly averaged wind data with either the highest or default data quality codes. Buoy winds are adjusted to 10-m height following Monin–Obukhov similarity theory (Zeng et al. 1998). An inverse-weighting scheme that accounts for distance between satellite footprint center and buoy location, time between the two different measurements, and buoy wind speed is applied to the satellite measurements following Boutin and Etcheto (1990). Then the

precipitation rate measured by each buoy equipped with a rain gauge is examined.

Figure 1 shows the results of this analysis. There was a total of 5,902 matchups between 18 March 2017 and 31 December 2018. While there were relatively few wind estimates with rainfall rates greater than 5 mm h^{-1} , CYGNSS shows very little impact from increased rainfall rates. The best-fit line has a slightly positive slope of $0.003 \text{ m s}^{-1} (\text{mm h}^{-1})^{-1}$, but the quality of fit is poor (correlation coefficient of 0.002) and nearly equal numbers of positively and negatively biased wind measurements exist at rain rates above 5 mm h^{-1} . The range of difference values is also similar regardless of rain rate. Asgarimehr et al. (2018) found that some rain effects can be seen in GNSS-R datasets, especially at low wind speeds ($<6 \text{ m s}^{-1}$). Disaggregating Fig. 1 by wind speed range (not shown) indicated a possibly similar positive bias in CYGNSS wind speeds in low-wind raining situations, but the number of available buoy matchups are even smaller than those available in Fig. 1, so confidence in this inference is low. Regardless, it is clear from Fig. 1 that any possible rain influence on CYGNSS observations is significantly smaller than the inherent uncertainty in the wind estimates themselves.

In summary, CYGNSS winds show little to no bias in the presence of rain when compared to buoys. Therefore, the ability of CYGNSS to operate successfully in the presence of rain is confirmed.

Wind speed uncertainty and resolution. WIND SPEED RETRIEVAL UNCERTAINTY $> 20 \text{ m s}^{-1}$. The assessment of YSLF wind speed retrieval uncertainty above 20 m s^{-1} follows a similar approach to that presented in (Ruf et al. 2018b). That assessment used an earlier version (v2.0) of the CYGNSS data products. Here, we use the more recent v2.1 products, for which a number

of improvements to the data calibration have been made, as described in Gleason et al. (2018) and Ruf and Balasubramaniam (2018). Matchups are compiled between CYGNSS and NOAA “hurricane hunter” aircraft measurements from 20 coincident storm overpasses during the 2017 Atlantic hurricane season. Aircraft flight lines were aligned during eyewall penetrations with CYGNSS specular point tracks. Coincidence is defined by requiring that aircraft and CYGNSS tracks occur within 30 min and 12.5 km of one another. The 20 coincident tracks include overpasses of Hurricanes Harvey on day of year (DOY) 236 (four tracks) and DOY 237; Irma on DOY

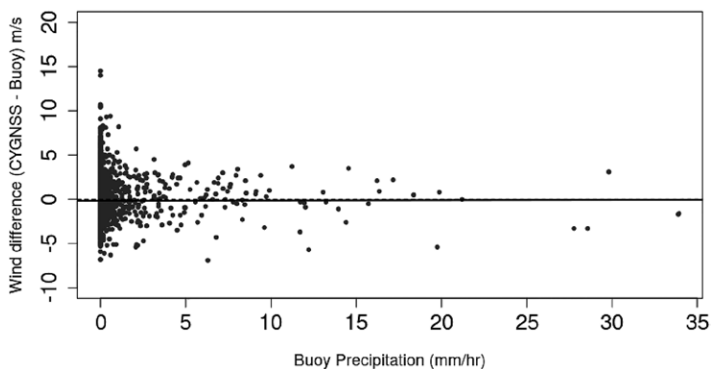


FIG. 1. Scatterplot of CYGNSS winds at the analyzed buoys (negative means buoy values are higher) as functions of buoy precipitation rate at the same locations. Also shown is the best-fit line.

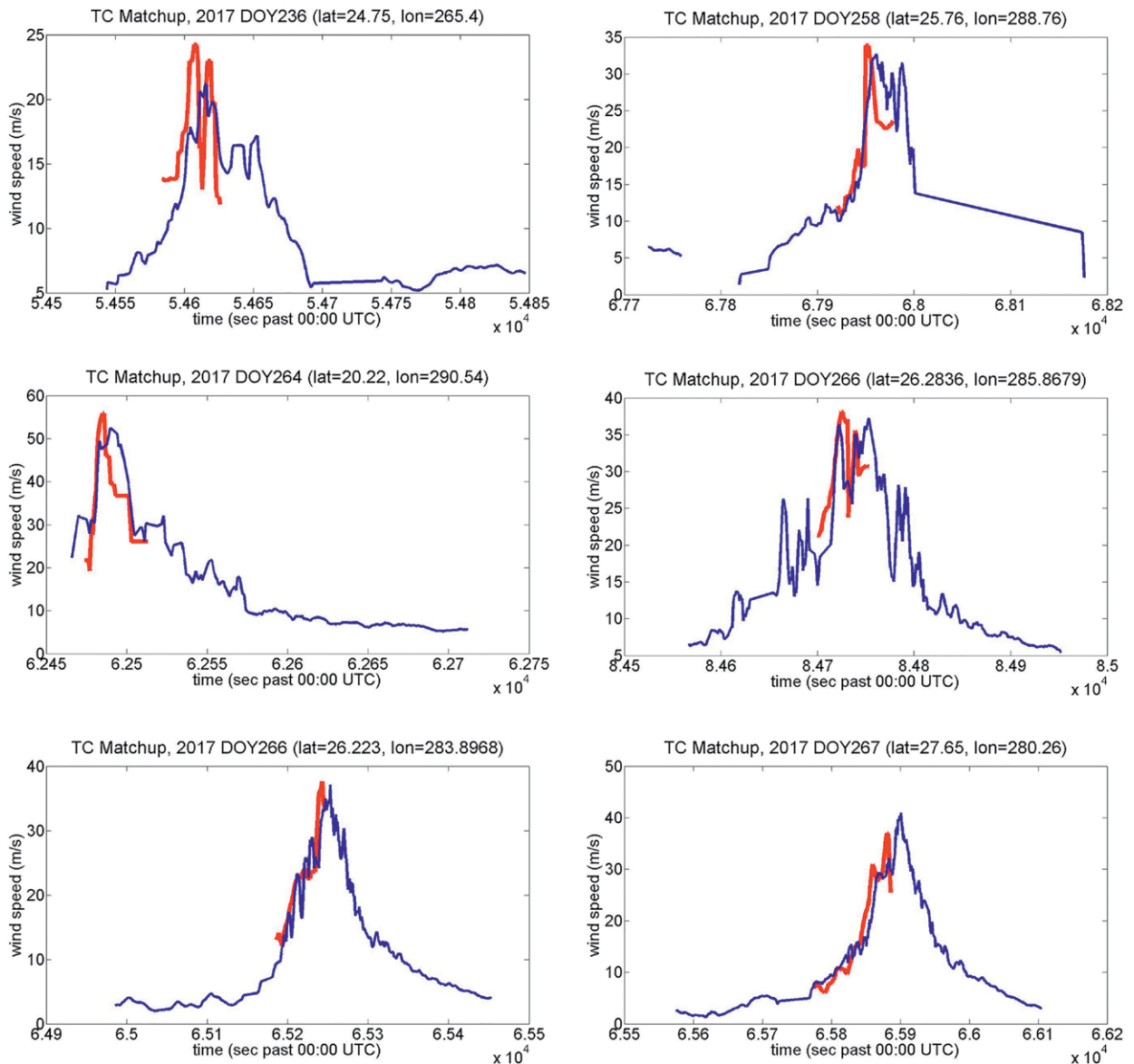


FIG. 2. Examples of CYGNSS overpasses of Hurricanes Harvey, Jose, and Maria during 2017 that were coincident with NOAA hurricane hunter aircraft flights. In each case, the storm, day of year (DOY) of the measurement, the incidence angle of the overpass, and the spatial resolution corresponding to that incidence angle are (top left) Harvey: DOY 236, 32.7°, and 22 km; (top right) Jose: DOY 258, 65.1°, and 36 km; (middle left) Jose: DOY 264, 58.1°, and 33 km; (middle right) Maria (pass 1): DOY 266, 64.2°, and 35 km; (bottom left) Maria (pass 2): DOY 266, 58.3°, and 33 km; and (bottom right) Maria: DOY 267, 54.9°, and 31 km. SFMR measurement of u_{10} are shown in red and CYGNSS measurements are shown in blue. SFMR tracks are truncated in time to meet the 30-min and 12.5-km collocation requirements.

248; Jose on DOY 258 (two tracks), DOY 259, and DOY 264 (four tracks); and Maria on DOY 266 (two tracks), DOY 267 (four tracks), and DOY 270. Comparison wind speeds were measured by SFMRs installed on the aircraft. A histogram of the SFMR wind speeds measured during the overpasses is shown in Fig. ES1 (see online supplement at <https://doi.org/10.1175/BAMS-D-18-0337.2>). The maximum wind speed in the histogram is 54 m s^{-1} (120 mph, category 3).

Examples of six of the hurricane overpasses are shown in Fig. 2. Both the winds retrieved by CYGNSS and measured by SFMR on the aircraft are shown.

A scatterplot with all wind speed matchups between CYGNSS and SFMR is shown in Fig. ES2a and a histogram of the difference between each pair of wind speeds is shown in Fig. ES2b (see online supplement). Considering only samples for which SFMR wind speed is greater than 20 m s^{-1} , the RMS

difference between CYGNSS and SFMR is 5.2 m s^{-1} and the mean difference (bias) is 1.0 m s^{-1} . When an uncertainty of 4 m s^{-1} for the SFMR measurements is removed (by root-sum-square subtraction), the remaining error ascribed to CYGNSS is 3.2 m s^{-1} . The mean value of the SFMR wind speeds is 28.8 m s^{-1} , so the relative CYGNSS uncertainty is 11.3% ($=3.2/28.8$). Note that the derived uncertainty in CYGNSS high wind retrievals depends on the uncertainty assumed for SFMR. The value of 4 m s^{-1} is based on the results by Uhlhorn et al. (2007). If a lower value were assumed, for example, the derived uncertainty allocated to CYGNSS would be higher.

WIND SPEED RETRIEVAL UNCERTAINTY < 20 m s^{-1} . For winds below 20 m s^{-1} , the CYGNSS FDS winds are compared to u_{10} winds from the GDAS 6-hourly 0.25° blended vector sea surface winds (Zhang et al. 2006; www.ncdc.noaa.gov/data-access/marineocean-data/blended-global/blended-sea-winds). All CYGNSS data from June 2017 through October 2018 are used. The CYGNSS data are filtered using the level 2 quality flags and are compared to GDAS winds, which are matched to the CYGNSS observations using nearest neighbor interpolation. The total number of CYGNSS/GDAS pairs is 67,967,456.

The level 2 quality flags test for a number of problems, any one of which will result in a data sample being excluded. The tests include 1) retrieved wind speeds below -5 m s^{-1} , 2) difference between wind speed retrieved from the scattering cross section and from the radar return waveform (leading edge slope) differing by more than 10 m s^{-1} , and 3) specular reflection lying outside of the range of adequate receive antenna gain. In practice, these filters typically remove a few percent of the total samples.

A density scatterplot of the matchups is shown in Fig. 3a. The areas of highest density in CYGNSS–GDAS matchups lie along the one-to-one line, indicating good agreement between the two estimates, with the highest density around 7 m s^{-1} , as is expected given the distribution of global ocean winds, which is generally Rayleigh distributed with a peak near 7 m s^{-1} . Note that there are also some areas of relatively high density away from the one-to-one line, for example, the high-density “lobes” for high wind estimates from either source.

The mean and RMS differences between CYGNSS and GDAS “ground truth” winds are shown in Fig. 3b. For winds below $\sim 7 \text{ m s}^{-1}$, the bias (GDAS – CYGNSS) is negative, indicating an overestimate by CYGNSS relative to GDAS for low winds, where the RMS difference is relatively constant at around 2 m s^{-1} . The

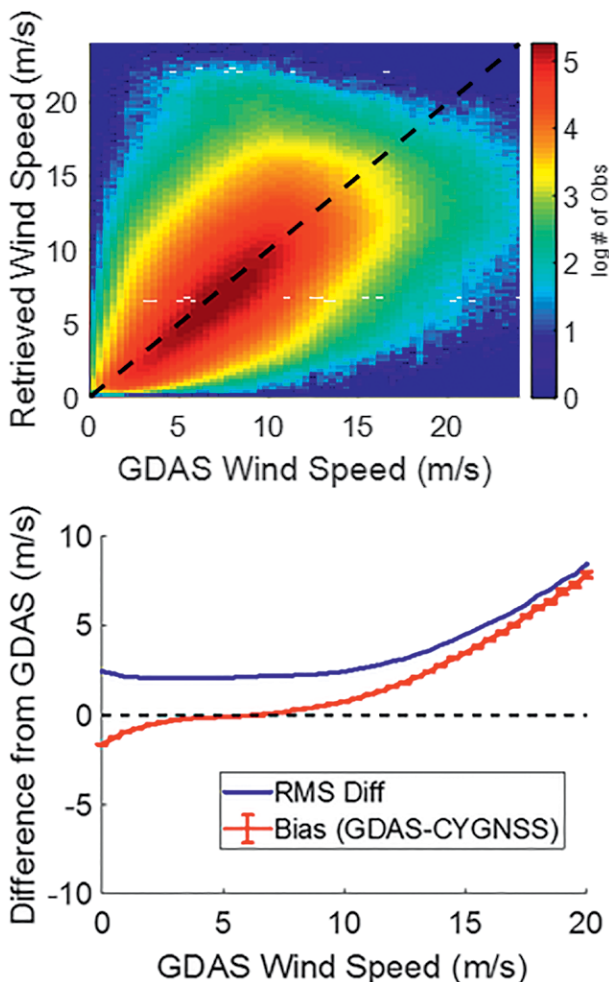


FIG. 3. (a) Log(density) scatterplot of CYGNSS and matchup GDAS wind speed samples used for estimating wind speed retrieval uncertainty below 20 m s^{-1} . The diagonal black dashed line is the line of 1:1 agreement. The color scale is the \log_{10} of the number density of points. (b) RMS (blue line) and mean (red line) difference between collocated CYGNSS and GDAS winds below 20 m s^{-1} as a function of GDAS wind speed. The 95% confidence limit error bars are shown for the mean values, but they are very small because the total number of observations is ~ 68 million. The results are computed over a $\pm 0.5 \text{ m s}^{-1}$ bin widths every 1 m s^{-1} .

bias becomes positive above the peak in the wind distribution at 7 m s^{-1} , indicating an underestimate by CYGNSS relative to GDAS for higher winds, with both the bias and the RMS difference increasing significantly as a function of wind speed above $\sim 10 \text{ m s}^{-1}$. The sensitivity of the CYGNSS measurements decreases with increasing wind speed, resulting in higher overall uncertainty in the CYGNSS estimates at higher wind speeds. While both the bias and RMS differences approach 8 m s^{-1} at wind speeds of 20 m s^{-1} , the overall uncertainty is weighted by the global distribution

of winds, which has a maximum likelihood near 7 m s^{-1} . The total RMS difference between CYGNSS and GDAS for winds below 20 m s^{-1} is 2.31 m s^{-1} . This includes not just uncertainties in the CYGNSS retrievals, but also uncertainties in the GDAS estimates and uncertainties in the spatiotemporal matchup of the two. Peng et al. (2013) estimate the uncertainty of the GDAS blended winds to be approximately 1.6 m s^{-1} . Likewise, in a comparison with buoy data, Yu and Gerald (2004) estimate GDAS surface wind RMS uncertainties of 1.8 m s^{-1} . Neglecting the matchup uncertainty term, this places an upper bound on the CYGNSS retrieval uncertainty for winds $< 20 \text{ m s}^{-1}$ of $\sim 1.67 \text{ m s}^{-1}$ from root-difference-square subtraction. This is below the CYGNSS requirement of 2 m s^{-1} uncertainty for wind speeds below 20 m s^{-1} . Note that, while the average uncertainty below 20 m s^{-1} is less than 2 m s^{-1} , it does rise above that level at the higher end of the range. Note also that the estimate of CYGNSS uncertainty is sensitive to the assumed error in GDAS and will increase as the assumed error in GDAS decreases.

The increase in retrieval bias and RMS difference with increasing wind speed is examined in Ruf et al. (2018b) and found to result from several factors. The primary one is a decrease in sensitivity with increasing wind speed. The geophysical model function (GMF) that maps normalized bistatic radar cross section (NB RCS) to u_{10} is nonlinear and exhibits a decreasing slope with increasing wind speed, with the result that the same uncertainty in measured NB RCS will cause a larger uncertainty in estimated u_{10} at high wind speed than at low wind speed.

A second, independent assessment of FDS wind speed uncertainty is also performed using matchups with coincident measurements by tropical buoys. Figure ES3 (see online supplement) shows the buoy–satellite matchup sample sizes at the tropical buoy locations. A total of 76 buoys were available after applying the matchup criteria described in the “Operation in the presence of rain” section, leading to an aggregated sample size of 12,164. The buoy array provides in situ wind speed values from the Indian, Pacific, and Atlantic Oceans, with most buoys lying equatorward of 15° . After restricting the CYGNSS winds to be below 20 m s^{-1} , the total number of samples is reduced to 12,155.

A 2D density scatterplot of the collocated samples is shown in Fig. 4a. The statistical metrics of root-mean-square difference (RMSD), standard deviation difference, correlation coefficient, and mean bias between CYGNSS and buoys are given in the figure. The scatterplot demonstrates a linear relationship

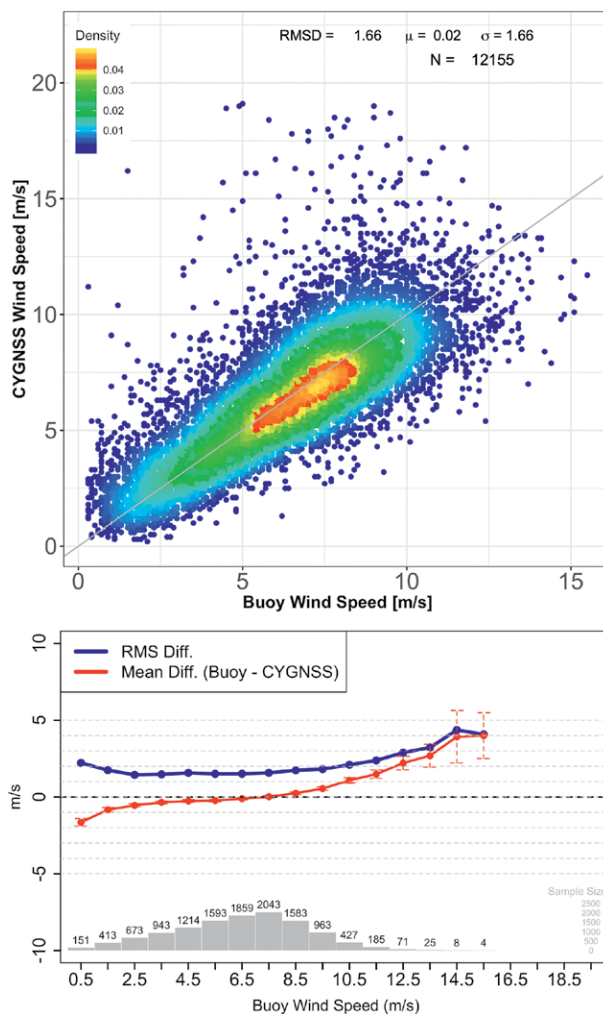


FIG. 4. (a) A 2D density plot of collocated CYGNSS and tropical buoy wind speeds. The diagonal gray line is the 1:1 agreement. The statistical parameters RMSD, μ , σ , and N are the root-mean-square difference (buoy – CYGNSS), mean bias, standard deviation of the difference, and the total sample size of the collocated CYGNSS and buoy wind data, respectively. (b) RMS (blue line) and mean (red line) difference between collocated CYGNSS and buoy wind speeds as a function of buoy wind speed. The error bars correspond to the 95% confidence limit. These metrics are computed over a $\pm 0.5 \text{ m s}^{-1}$ bin width for every 1 m s^{-1} buoy wind speed. Dashed horizontal lines tick the y axis at 1 m s^{-1} wind interval. The light gray bars and label on top of each bar indicate the sample size in each group of $\pm 0.5 \text{ m s}^{-1}$ bin width.

between CYGNSS and in situ observations. The highest density of points (reddish colors) lies along the 1:1 line concentrated within the wind range of $5\text{--}7 \text{ m s}^{-1}$, which is consistent with the previous study of Ruf et al. (2018b), although they used ECMWF as the observation reference. The RMSD is $\sim 1.7 \text{ m s}^{-1}$ and the mean bias is near zero. This upper bound

on CYGNSS retrieval uncertainty is consistent with the results reported above based on matchups between CYGNSS and GDAS. It is noteworthy that CYGNSS has slightly more measurements above 15 m s^{-1} than do the buoys, suggesting that CYGNSS may be biased in this high wind range—at these low latitudes, although the number of samples in this range is quite low (~ 50 for CYGNSS compared to ~ 5 for the buoys).

Figure ES4 (see online supplement) shows the frequency distribution of wind speed for CYGNSS and the buoys. Although the shape of the two distributions is very similar, there are some small but noticeable differences in some wind speed ranges, including a shift in the wind speed of maximum likelihood. For example, compared to the buoy values, CYGNSS exhibits an overestimation in the wind speed range of $\sim 3.5\text{--}6.5 \text{ m s}^{-1}$ and an underestimation in the higher wind speed range of $\sim 7.5\text{--}10.5 \text{ m s}^{-1}$.

Similar to the top-down analyses of Ruf et al. (2018b), the dependencies of the bias and RMSD between buoy and CYGNSS winds on the buoy wind speed values were analyzed and the results are shown in Fig. 4b. In general, the bias (buoy minus CYGNSS) is negative for low buoy wind speeds ($< \sim 6 \text{ m s}^{-1}$), near zero in the buoy wind range of $\sim 6\text{--}8 \text{ m s}^{-1}$, and becomes positive at higher wind speeds, growing to near $+4 \text{ m s}^{-1}$ at speeds near 15 m s^{-1} . Note that a very few collocated samples (< 10) are available at this wind range (Fig. 4b). The RMSD values remain below 2 m s^{-1} throughout the wind speed range of 2 to $\sim 10 \text{ m s}^{-1}$.

SPATIAL RESOLUTION. The spatial resolution of CYGNSS wind speed measurements is largely determined by the area of the surface bounded by the delay and Doppler ranges of the delay Doppler map (DDM) area (DDMA) used by the wind speed retrieval algorithm (Clarizia and Ruf 2016a). The DDMA includes propagation delays of up to 500 ns and Doppler shifts of up to 1,000 Hz relative to their values at the specular point (Gleason et al. 2018). We define the surface bounded by the DDMA as the instantaneous field of view (IFOV), which is consistent with the definition used by Clarizia and Ruf (2016a). The IFOV does not include the effects of the GPS spreading function, which increases the effective surface area. This can theoretically add up to 25% to the IFOV surface area (Clarizia and Ruf 2016b). However, empirical land crossing analysis (described below) shows the spatial resolution to be fairly close to the IFOV alone.

The IFOV is dependent on observatory altitude, with higher altitudes resulting in larger spatial

resolution. Figure ES5 (see online supplement) illustrates the IFOV as a function of incidence angle for the high- and low-altitude limits of the CYGNSS orbit. The IFOV exceeds the CYGNSS baseline requirement of 25 km for incidence angles higher than 39.6° and 36.3° at the lowest and highest altitudes, respectively. The resolution meets the threshold requirement of 50 km at all incidence angles.

Figure ES6 (see online supplement) illustrates how spatial resolution affects the CYGNSS mean daily coverage. Two versions of the calibration are considered. Version 2.1 calibration does not correct for transmit power fluctuations by the GPS block type IIF satellites, with the result that they are not included for wind speed retrievals. This reduces the mean daily coverage by approximately 37%. However, version 3.0 calibration is able to correct for these fluctuations, which increases the number of wind observations available and improves the mean daily coverage statistic. Figure ES6 shows that the CYGNSS baseline mean daily coverage requirement is met by v3.0 and the threshold requirement is met by v2.1.

As an overall estimate of CYGNSS spatial resolution, a weighted average is taken of the IFOV as a function of incidence angle, weighted by the distribution of observations at each incidence angle. This results in an overall spatial resolution for the NBRCS and the wind speed derived from it of 25.4 km.

For an empirical examination of the spatial resolution, we consider the effects of land on measurements over ocean near the coastline. Figure 5a shows a land–ocean–land CYGNSS track near the Florida Panhandle. The incidence angle of the observation is 15° . Measurements in the figure between sample times 44 and 51, at distances to land of $> 15 \text{ km}$, show negligible land contribution, suggesting that the IFOV shown in Fig. ES5 is a conservative estimate of spatial resolution.

As an additional demonstration of land contamination close to the coast, we consider a reflection track at a higher incidence angle of 44° , where the effects of land are more noticeable. Figure 5b shows the track moving south from the ocean to the Great Sandy Desert in northern Australia. Contamination from land contributions is clearly evident in the DDMA at roughly second 51. The green box in the figure (DDM 51) shows how the power changes due to land contributions. The integration end point of DDM 50 (start point of DDM 51) is roughly 28.5 km from the shoreline, which is consistent with the IFOV predicted in Fig. ES5 for an observation at an incidence angle of 44° .

A further examination of the spatial resolution over land under conditions of coherent reflection

from smooth inland water bodies is considered in the online supplement. In this case, the resolution improves significantly and varies between ~ 500 and $\sim 1,500$ m, depending on incidence angle, as shown in Fig. ES7 (see online supplement) and on the ground speed of the specular point motion, as shown in Fig. ES8 (see online supplement). One example of coherent specular reflection while crossing an inland water body is shown in Fig. ES9 (see online supplement).

Sampling properties. DUTY CYCLE OF SCIENCE OPERATIONS. The GPS science radar receivers on each CYGNSS spacecraft can operate in three data-taking modes. The “compressed DDM” mode produces four DDMs of surface scattering cross section per second. They are centered on the available specular points with highest measurement sensitivity and map the diffuse scattering within several tens of kilometers of the specular point. The “full DDM” mode measures scattering near the same four specular points but over a broader region, typically within several hundred kilometers of the specular point, and with higher precision (Gleason et al. 2016). The “raw IF” mode records a bit stream of raw data samples prior to any onboard processing. The full DDM and raw IF modes have data rates that are two and four orders of magnitude higher than that of the compressed DDM mode, respectively. They provide enhanced measurement quality during special science operations that are commanded from the ground. The compressed DDM mode is used most of the time and

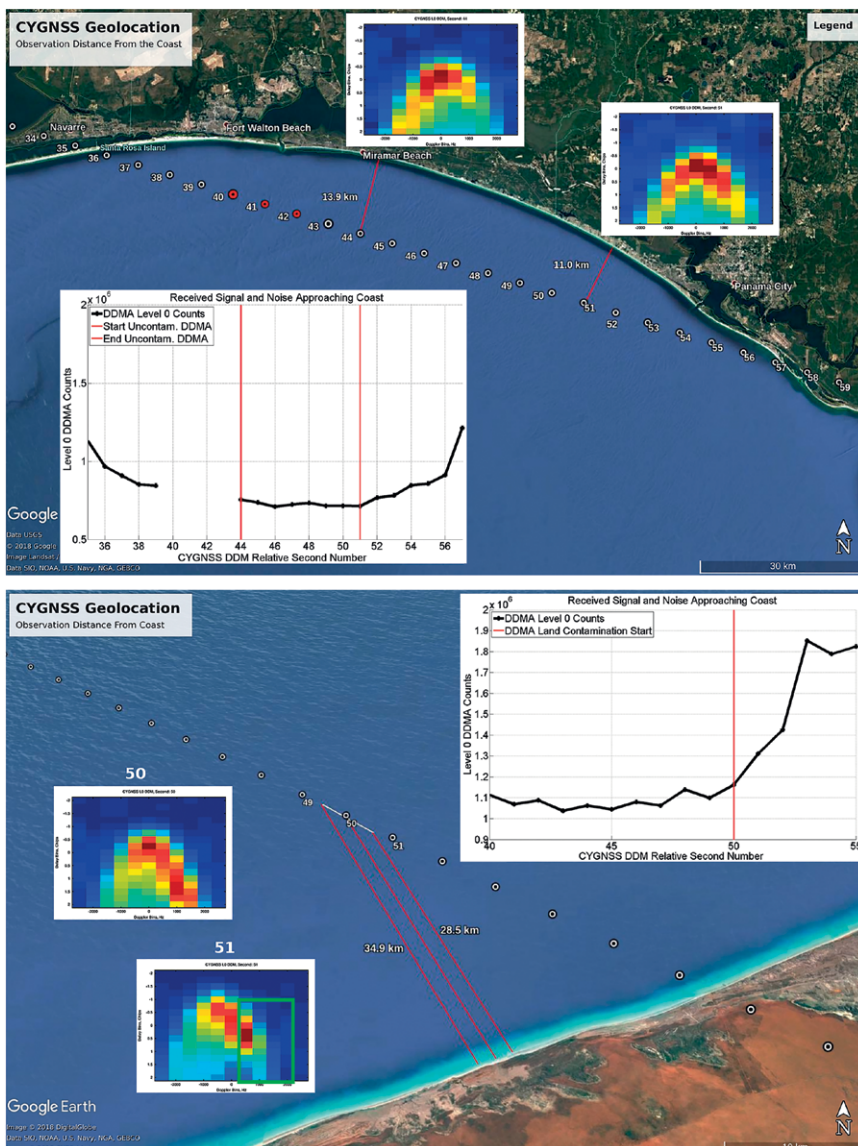


FIG. 5. (a) An oblique land–ocean–land CYGNSS track off the Florida Panhandle. In this case, the low observation incidence angle (approximately 15°) results in minor land contamination at distances of ~ 15 km from the shoreline. (b) Ocean–land crossing DDMA power fluctuations at 44° incidence. Land contributions are clearly evident in the DDMA at roughly second 50/51 in the track. The green box (DDM 51) indicates the DDM power changes due to land reflection contributions. The integration end point of DDM 50 (start point of DDM 51) is roughly 28.5 km from the shoreline, consistent with Fig. ES6.

its data products are assumed for all performance assessments considered here.

The spacecraft power, thermal, and data telemetry systems are all designed to support continuous operation in compressed DDM mode. All spacecraft operate in this mode except during autonomous recovery from unexpected anomalies or when performing differential drag adjustments to the intersatellite spacing of the constellation. Downlink data telemetry bandwidth is the primary factor that dictates

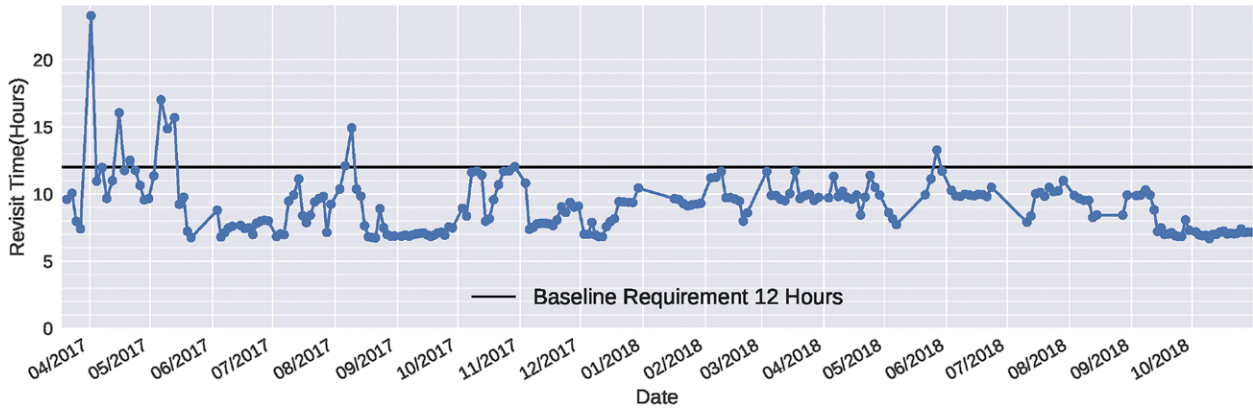


FIG. 6. Time series of CYGNSS L2 revisit time (blue) relative to the mission level requirement of 12 h (black). The mean revisit time for the entire mission is 9.1 h. A total of 231 revisit time samples were computed between 18 Mar 2017 and 31 Oct 2018 at time intervals for which spatial coverage is >70% (approximately every 46 h). The baseline requirement of 12 h was met by 96% of samples. Revisit time statistics are minimum = 6.68 h, maximum = 23.27 h, mean = 9.08 h, and standard deviation = 2.06 h.

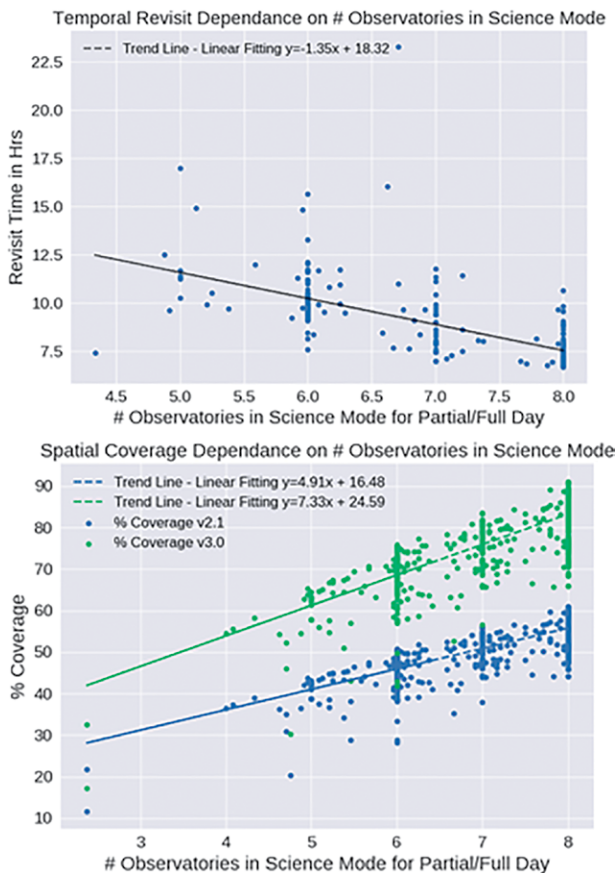


FIG. 7. CYGNSS sampling properties as a function of the number of observatory days (1 observatory day = 1 observatory operating for 1 full day) in nominal science data-taking mode. (a) Revisit time – mean time between samples of $\frac{1}{4}^\circ \times \frac{1}{4}^\circ$ bins within $\pm 35^\circ$ latitude. (b) Spatial coverage – fraction of $\frac{1}{4}^\circ \times \frac{1}{4}^\circ$ bins within $\pm 35^\circ$ latitude that are sampled in 24 h, broken out by science processing version 2.1 (blue) and version 3.0 projected (green).

operation in compressed DDM mode. It is possible to downlink all the compressed DDM data acquired over a continuous 48-h period using one contact with a ground station lasting ~ 8 min. Full DDM mode, with its two order of magnitude greater data rate, requires that much more ground contact time. Raw IF mode requires four orders of magnitude greater ground contact time. As a result, these special science modes are typically only used for brief periods of time while passing over target areas of interest. For example, full DDM and raw IF measurements have been made while passing over the inner core regions of tropical cyclones.

TEMPORAL REVISIT. Revisit time is defined here as the time separation between sequential measurements within the same $\frac{1}{4}^\circ \times \frac{1}{4}^\circ$ latitude–longitude bin by any CYGNSS observatory. The revisit times for every bin with more than one sample are averaged together to produce the reported mean revisit time. Bins with no resamples are not included in the average.

Figure 6 shows the revisit time over the life of the mission, with a histogram of the values shown in Fig. ES10 (see online supplement). The mean revisit time over the entire mission is 9.1 h, which meets the mission requirement of 12 h. All instances for which the requirement was exceeded occurred when multiple observatories were not in science mode due to high-drag maneuvers, safing events, or data loss due to onboard data processing anomalies. The dependence of revisit time on the number of observatories that are in science mode is shown in Fig. 7a. The dependence is fairly strong, with an approximately linear relationship between revisit time and number of observatories.

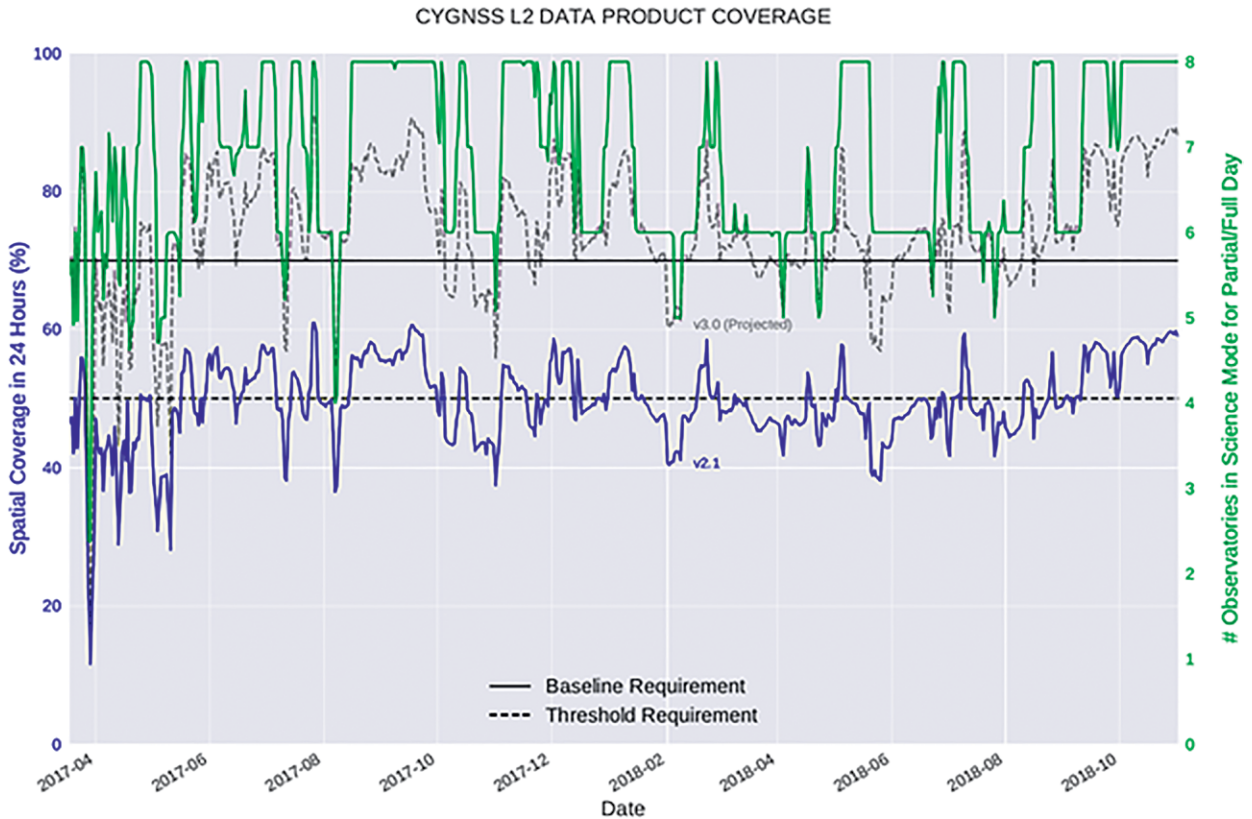


FIG. 8. Time series of CYGNSS spatial coverage for v2.1 (blue) and v3.0 (dashed) data along with number of observatory days (1 observatory day = 1 observatory operating for 1 full day) in science mode (green). Version 3.0 coverage is projected because this version is not scheduled for public release until later in 2019. There are a total of 685 daily spatial coverage samples between 18 Mar 2017 and 31 Oct 2018. 52% of v2.1 samples are above the threshold requirement of 50% coverage. Nearly all of v3.0 coverage samples will exceed the threshold requirement, and 77% will exceed the baseline requirement of 70% coverage. Coverage statistics for v2.1 are mean = 51%, median = 50%, standard deviation = 6%, minimum = 11%, and maximum = 61%. Statistics for v3.0 are mean = 75%, median = 74%, standard deviation = 9%, minimum = 17%, and maximum = 91%.

SPATIAL COVERAGE. Spatial coverage is defined as the percentage of $\frac{1}{4}^\circ \times \frac{1}{4}^\circ$ bins within $\pm 35^\circ$ latitude in which wind speeds are measured over 24 h. The baseline and threshold requirements are 70% and 50%, respectively. Spatial coverage for the mission to date is shown in Fig. 8. The latest version of CYGNSS data, v2.1, released on 21 September 2018 (blue data in Fig. 8), provides a mean of 50% spatial coverage, meeting the threshold requirement. Version 2.1 data excludes any observations using block type IIF GPS satellites, removing approximately 37% of the available data. Version 3.0 (dashed data in Fig. 8), which is under development, will include near-real-time estimates of GPS transmitted power from the CYGNSS zenith antenna measurements. This will allow for the inclusion of block type IIF data. Spatial coverage is projected to rise to 74% with this update, exceeding the mission baseline requirement of 70%. There is a strong correlation between the number of observatories in science mode (green data in Fig. 8) and spatial

coverage. Figure 7b shows the dependence of spatial coverage on the number of observatories in science mode for the current v2.1 data as well as projections for the upcoming v3.0 data. As with revisit time, this dependence is fairly strong, with a roughly linear relationship between the two. Maps of the typical coverage provided by the complete constellation of eight observatories over one orbit and one day are shown in Fig. 9.

DATA LATENCY. Data latency is defined as the elapsed time between the downlink of raw CYGNSS data at a ground station and the availability of calibrated science data products at the PO.DAAC. There is no L1 mission science requirement for this metric, but there is an expectation that the data latency will remain under 6 days. Since the release of v1.1 data in June 2017, the mean data latency has been 2.7 days. Automation of science processing, begun in January 2018, has further reduced the mean data latency to 2.1 days.

Cal/val activities. Calibration and validation (cal/val) activities for the CYGNSS mission have focused on its primary level 1 and level 2 science data products. The primary L1 product is the NBRCS of the ocean surface and the primary L2 product is u_{10} . Postlaunch efforts to calibrate the NBRCS have improved characterization of the signals transmitted by each GPS satellite (Wang et al. 2018), improved characterization of the radar receiver hardware on each CYGNSS satellite, and refined the calibration of signal power received by the radars. Overall NBRCS measurement uncertainty is ± 0.4 -dB RMS (Gleason et al. 2018).

Calibration of the u_{10} data products consists of developing a geophysical model function (GMF) that maps NBRCS to u_{10} . Development of the GMF is described in detail in Ruf and Balasubramaniam (2018). The GMF is used by the wind speed retrieval algorithm to estimate u_{10} from measurements of NBRCS (Clarizia and Ruf 2016a). Validation of the u_{10} data products is performed by statistical comparisons between the CYGNSS measurements and independent measurements of u_{10} that are nearly coincident in space and time. Below 20 m s^{-1} , the comparisons are made with GDAS reanalysis numerical model predictions. Above 20 m s^{-1} , they are made with measurements made by the SFMR instruments on NOAA P-3 “hurricane hunter” aircraft, which flew coordinated eyewall penetrations of hurricanes at the same time and along the same track as CYGNSS overpasses of the storms. Details of both comparisons are given above, in the “Wind speed retrieval uncertainty $> 20 \text{ m s}^{-1}$ ” and “Wind speed retrieval uncertainty $< 20 \text{ m s}^{-1}$ ” sections.

Hurricane operations support. CYGNSS is a research, as opposed to operational, mission. Its primary objectives focus on producing science data products with specific spatial and temporal resolution and measurement uncertainty. The data products support a number of science investigations, including TC process studies, characterizing air–sea surface fluxes, understanding tropical convection dynamics, modeling and forecasting storm surge, and, over land, measuring surface soil moisture and mapping flood inundation. Several of the investigations also examine the potential for CYGNSS measurements to be used in support of hurricane operations. The

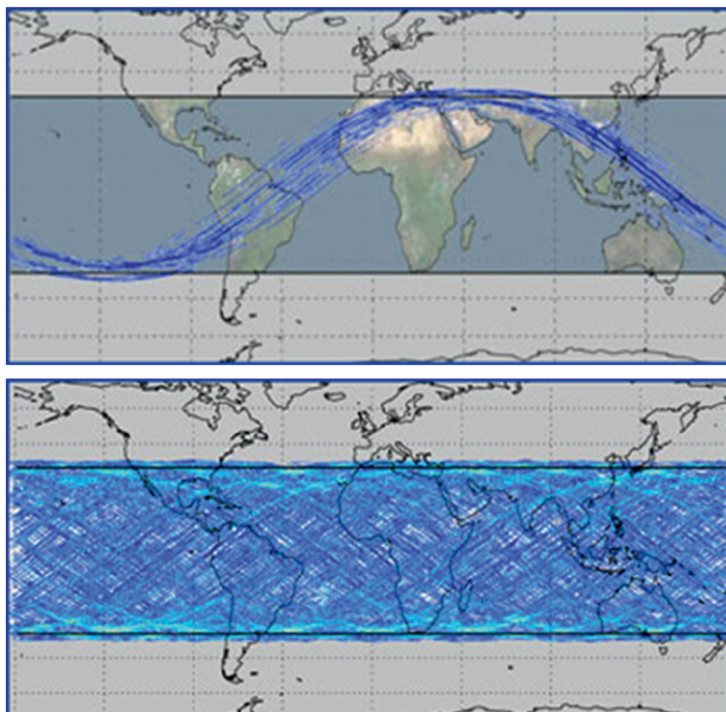


FIG. 9. Typical coverage maps for the complete constellation of eight observatories after (top) one 95-min orbit and (bottom) over a complete 24-h interval.

potential impact of CYGNSS wind speed measurements on numerical hurricane forecasts has been examined using observing system simulation experiments (OSSEs) (McNoldy et al. 2017; Annane et al. 2018; Leidner et al. 2018). In each OSSE investigation, the potential was demonstrated, using simulated CYGNSS measurements in the inner core of TCs, for a significant positive impact on hurricane track and intensity forecast skill.

Since the CYGNSS launch and completion of its early on-orbit commissioning and calibration, case studies have been conducted of the impact on forecast skill of assimilating actual flight data into the operational Hurricane Weather Research and Forecasting Model (HWRF). These studies “replay” some of the major 2017 Atlantic hurricanes and examine the differences between forecasts made with and without CYGNSS data included (Annane et al. 2019; Cui et al. 2019a,b). In each case, positive impacts on forecast skill are demonstrated when CYGNSS observations are added to the standard suite of observations input to HWRF. However, these studies are still in their early stages. More refined methods of data assimilation and more comprehensive evaluations of performance are expected before CYGNSS wind speed measurements are ready to be used on an operational basis by HWRF or other operational numerical forecast models.

SUMMARY AND CONCLUSIONS.

CYGNSS performance relative to its L1 mission science requirements is summarized in Table 2. The current best estimate (CBE) of performance is reported and compared to each L1 requirement. Cases where the baseline requirement is met or exceeded necessarily also exceed the threshold requirement. Cases where the baseline requirement is not met but the threshold is are so noted. In all cases but one, either the baseline or threshold requirement is met or exceeded. The one outlier case is wind speed retrieval uncertainty at wind speeds above 20 m s^{-1} . The common baseline and threshold requirement is an uncertainty of 10%. The current CBE performance is an uncertainty of 11.3%.

L1 mission science performance is expected to improve as a result of planned future improvements to calibration and data processing. In particular, the upgrade to v3.0 calibration, which will include a real-time correction for variations in the transmit power of the GPS satellites, is expected to improve the temporal and spatial sampling properties of the constellation as well as the accuracy of NBRCS calibration. This should, in turn, reduce the uncertainty in the wind speed retrievals at both high and low wind speed levels. Whether the high wind speed uncertainty will be lowered below the 10% requirement level remains to be seen. However, the preliminary results of data assimilation into HWRF (e.g., in Cui et al. 2019b) suggest that, even at the current 11.3% level of uncertainty, there is already useful information about the TC inner core wind field contained in CYGNSS measurements. The CYGNSS wind measurements during TC overpasses may also improve the characterization of storm wind structure, and estimation of significant wind radii. This is an area of active research by the project (Morris and Ruf 2017; Krien et al. 2018).

ACKNOWLEDGMENTS. The work presented was supported in part by NASA Science Mission Directorate Contract NNL13AQ00C with the University of Michigan. DEW's contributions to this study were carried out on behalf of the Jet Propulsion Laboratory, California Institute of Technology, under a contract with the National Aeronautics and Space Administration.

TABLE 2. CYGNSS level 1 mission science performance.

No.	Requirement	CBE	Satisfies requirement?
1	Wind speed dynamic range at $5 \text{ km} \times 5 \text{ km}$ resolution	54 m s^{-1}	Exceeds threshold
2	Operation in presence of rain	Yes	Meets baseline
3a	Retrieval uncertainty for winds $> 20 \text{ m s}^{-1}$	11.3%	10% requirement
3b	Retrieval uncertainty for winds $< 20 \text{ m s}^{-1}$	1.67 m s^{-1}	Exceeds baseline
3c	Spatial resolution	25.4 km	Exceeds threshold
4a	100% duty cycle during science operations	Yes	Meets baseline
4b	Mean temporal resolution	9.1 h	Exceeds baseline
4c	Spatial sampling coverage of cyclone historical tracks in 24 h	50%–74%	Exceeds threshold
5	Calibrate and validate CYGNSS data in individual wind speed bins above and below 20 m s^{-1}	Yes	Meets baseline
6	Support operational hurricane forecast community	Yes	Meets baseline

REFERENCES

- Annane, B., B. McNoldy, S. Leidner, R. Hoffman, R. Atlas, and S. Majumdar, 2018: A study of the HWRF analysis and forecast impact of realistically simulated CYGNSS observations assimilated as scalar wind speeds and as VAM wind vectors. *Mon. Wea. Rev.*, **146**, 2221–2236, <https://doi.org/10.1175/MWR-D-17-0240.1>.
- , —, —, —, —, and —, 2019: Impact of CYGNSS ocean surface wind speeds on analysis and forecasts of Hurricane Harvey and Irma (2017) with HWRF model. *23rd Conf. on Integrated Observing and Assimilation Systems for the Atmosphere, Oceans, and Land Surface*, Phoenix, AZ, Amer. Meteor. Soc., 11.3, <https://ams.confex.com/ams/2019Annual/meetingapp.cgi/Paper/351493>.
- Asgarimehr, M., V. Zavorotny, J. Wickert, and S. Reich, 2018: Can GNSS reflectometry detect precipitation over oceans? *Geophys. Res. Lett.*, **45**, 12 585–12 592, <https://doi.org/10.1029/2018GL079708>.
- Bourles, B., and Coauthors, 2008: The PIRATA program: History, accomplishments, and future directions. *Bull. Amer. Meteor. Soc.*, **89**, 1111–1125, <https://doi.org/10.1175/2008BAMS2462.1>.
- Boutin, J., and J. Etcheto, 1990: Seasat scatterometer versus scanning multichannel microwave radiometer wind speeds: A comparison on a global scale. *J. Geophys. Res.*, **95**, 22 275–22 288, <https://doi.org/10.1029/JC095iC12p22275>.
- Chen, D. D., C. S. Ruf, and S. T. Gleason, 2016: Response time of mean square slope to wind forcing: An

- empirical investigation. *J. Geophys. Res. Oceans*, **121**, 2809–2823, <https://doi.org/10.1002/2016JC011661>.
- Chew, C., J. T. Reader, and E. Small, 2018: CYGNSS data map flood inundation during the 2017 Atlantic hurricane season. *Sci. Rep.*, **8**, 9336, <https://doi.org/10.1038/s41598-018-27673-x>.
- Clarizia, M. P., and C. S. Ruf, 2016a: Wind speed retrieval algorithm for the Cyclone Global Navigation Satellite System (CYGNSS) Mission. *IEEE Trans Geosci. Remote Sens.*, **54**, 4419–4432, <https://doi.org/10.1109/TGRS.2016.2541343>.
- , and —, 2016b: On the spatial resolution of GNSS reflectometry. *IEEE Trans Geosci. Remote Sens. Lett.*, **13**, 1064–1068, <https://doi.org/10.1109/LGRS.2016.2565380>.
- Cui, Z., Z. Pu, C. Ruf, and V. Tallapragada, 2019a: Impact of CYGNSS data on tropical cyclone analysis and forecasts using the operational HWRF. *23rd Conf. on Integrated Observing and Assimilation Systems for the Atmosphere, Oceans, and Land Surface*, Phoenix, AZ, Amer. Meteor. Soc., 11.5, <https://ams.confex.com/ams/2019Annual/webprogram/Paper351968.html>.
- , —, V. Tallapragada, R. Atlas, and C. S. Ruf, 2019b: A preliminary impact study of CYGNSS ocean surface wind speeds on numerical simulations of hurricanes. *Geophys. Res. Lett.*, **46**, 2984–2992, <https://doi.org/10.1029/2019GL082236>.
- Draper, D. W., and D. G. Long, 2004a: Evaluating the effect of rain on SeaWinds scatterometer measurements. *J. Geophys. Res.*, **109**, C02005, <https://doi.org/10.1029/2002JC001741>.
- , and —, 2004b: Simultaneous wind and rain retrieval using SeaWinds data. *IEEE Trans. Geosci. Remote Sens.*, **42**, 1411–1423, <https://doi.org/10.1109/TGRS.2004.830169>.
- Gleason, S., C. Ruf, M. P. Clarizia, and A. O'Brien, 2016: Calibration and unwrapping of the normalized scattering cross section for the Cyclone Global Navigation Satellite System (CYGNSS). *IEEE Trans. Geosci. Remote Sens.*, **54**, 2495–2509, <https://doi.org/10.1109/TGRS.2015.2502245>.
- , —, A. O'Brien, and D. S. McKague, 2018: The CYGNSS level 1 calibration algorithm and error analysis based on on-orbit measurements. *IEEE J. Sel. Top. Appl. Earth Obs. Remote Sens.*, **12**, 37–49, <https://doi.org/10.1109/JSTARS.2018.2832981>.
- Jensen, K., K. McDonald, E. Podest, N. Rodriguez-Alvarez, V. Horna, and N. Steiner, 2018: Assessing L-band GNSS-reflectometry and imaging radar for detecting sub-canopy inundation dynamics in a tropical wetlands complex. *Remote Sens.*, **10**, 1431, <https://doi.org/10.3390/rs10091431>.
- Kim, H., and V. Lakshmi, 2018: Use of Cyclone Global Navigation Satellite System (CYGNSS) observations for estimation of soil moisture. *Geophys. Res. Lett.*, **45**, 8272–8282, <https://doi.org/10.1029/2018GL078923>.
- Krien, Y., and Coauthors, 2018: Can we improve parametric cyclonic wind fields using recent satellite remote sensing data? *Remote Sens.*, **10**, 1963, <https://doi.org/10.3390/rs10121963>.
- Leidner, S., B. Annane, B. McNoldy, R. Hoffman, and R. Atlas, 2018: Variational analysis of simulated ocean surface winds from the Cyclone Global Navigation Satellite System (CYGNSS) and evaluation using a regional OSSE. *J. Atmos. Oceanic Technol.*, **35**, 1571–1584, <https://doi.org/10.1175/JTECH-D-17-0136.1>.
- Marzano, F., L. Roberti, and A. Mugnai, 2000: Impact of rainfall incoherent backscattering upon radar echoes above 10 GHz. *Phys. Chem. Earth*, **25**, 943–948, [https://doi.org/10.1016/S1464-1909\(00\)00130-1](https://doi.org/10.1016/S1464-1909(00)00130-1).
- McNoldy, B., B. Annane, S. Majumdar, J. Delgado, L. Bucci, and R. Atlas, 2017: Impact of assimilating CYGNSS data on tropical cyclone analyses and forecasts in a regional OSSE framework. *Mar. Technol. Soc. J.*, **51**, 7–15, <https://doi.org/10.4031/MTSJ.51.1.1>.
- McPhaden, M. J., and Coauthors, 1998: The Tropical Ocean-Global Atmosphere (TOGA) observing system: A decade of progress. *J. Geophys. Res.*, **103**, 14 169–14 240, <https://doi.org/10.1029/97JC02906>.
- , and Coauthors, 2009: RAMA: The Research Moored Array for African–Asian–Australian Monsoon Analysis and Prediction. *Bull. Amer. Meteor. Soc.*, **90**, 459–480, <https://doi.org/10.1175/2008BAMS2608.1>.
- Meissner, T., L. Ricciardulli, and F. J. Wentz, 2017: Capability of the SMAP mission to measure ocean surface winds in storms. *Bull. Amer. Meteor. Soc.*, **98**, 1660–1677, <https://doi.org/10.1175/BAMS-D-16-0052.1>.
- Milliff, R. F., J. Morzel, D. B. Chelton, and M. H. Freilich, 2004: Wind stress curl and wind stress divergence biases from rain effects on QSCAT surface wind retrievals. *J. Atmos. Oceanic Technol.*, **21**, 1216–1231, [https://doi.org/10.1175/1520-0426\(2004\)021<1216:WSCAWS>2.0.CO;2](https://doi.org/10.1175/1520-0426(2004)021<1216:WSCAWS>2.0.CO;2).
- Morris, M., and C. S. Ruf, 2017: Determining tropical cyclone surface wind speed structure and intensity with the CYGNSS satellite constellation. *J. Appl. Meteor. Climatol.*, **56**, 1847–1865, <https://doi.org/10.1175/JAMC-D-16-0375.1>.
- Nie, C., and D. G. Long, 2007: A C-band wind/rain backscatter model. *IEEE Trans. Geosci. Remote Sens.*, **45**, 621–631, <https://doi.org/10.1109/TGRS.2006.888457>.
- , and —, 2008: A C-band scatterometer simultaneous wind/rain retrieval method. *IEEE Trans. Geosci. Remote Sens.*, **46**, 3618–3632, <https://doi.org/10.1109/TGRS.2008.922146>.

- Nielsen, S., and D. G. Long, 2009: Wind and rain backscatter model derived from AMSR and SeaWinds data. *IEEE Trans. Geosci. Remote Sens.*, **47**, 1595–1606, <https://doi.org/10.1109/TGRS.2008.2007492>.
- Owen, M. P., and D. G. Long, 2011: Simultaneous wind and rain estimation for QuikSCAT at ultra-high resolution. *IEEE Trans. Geosci. Remote Sens.*, **49**, 1865–1878, <https://doi.org/10.1109/TGRS.2010.2102361>.
- Peng, G., H.-M. Zhang, H. P. Frank, J.-R. Bidlot, M. Higaki, S. Stevens, and W. R. Hankins, 2013: Evaluation of various surface wind products with OceanSITES buoy measurements. *Wea. Forecasting*, **28**, 1281–1303, <https://doi.org/10.1175/WAF-D-12-00086.1>.
- PO.DAAC, 2018: CYGNSS. NASA Physical Oceanography Distributed Active Archive Center, <https://podaac.jpl.nasa.gov/CYGNSS>.
- Pu, Z., Z. Cui, S. Zhang, and C. Yu, 2018: Enhancing tropical cyclone prediction with advanced assimilation of GPM and CYGNSS satellite observations. *15th Annual Meeting*, Honolulu, Hawaii, Asia Oceania Geosciences Society.
- Ruf, C., and R. Balasubramaniam, 2018: Development of the CYGNSS geophysical model function for wind speed. *IEEE J. Sel. Top. Appl. Earth Obs. Remote Sens.*, **12**, 66–77, <https://doi.org/10.1109/JSTARS.2018.2833075>.
- , and Coauthors, 2016: New ocean winds satellite mission to probe hurricanes and tropical convection. *Bull. Amer. Meteor. Soc.*, **97**, 385–395, <https://doi.org/10.1175/BAMS-D-14-00218.1>.
- , C. Chew, T. Lang, M. G. Morris, K. Nave, A. Ridley, and R. Balasubramaniam, 2018a: A new paradigm in Earth environmental monitoring with the CYGNSS small satellite constellation. *Sci. Rep.*, **8**, 8782, <https://doi.org/10.1038/s41598-018-27127-4>.
- , S. Gleason, D. S. McKague, 2018b: Assessment of CYGNSS wind speed retrieval uncertainty. *IEEE J. Sel. Topics Appl. Earth Obs. Remote Sens.*, **12**, 87–97, <https://doi.org/10.1109/JSTARS.2018.2825948>.
- Tournadre, J., and Y. Quilfen, 2003: Impact of rain cell on scatterometer data: 1. Theory and modeling. *J. Geophys. Res.*, **108**, 3225, <https://doi.org/10.1029/2002JC001428>.
- Uhlhorn, E. W., P. G. Black, J. L. Franklin, M. A. Goodberlet, J. R. Carswell, and A. S. Goldstein, 2007: Hurricane surface wind measurements from an operational stepped frequency microwave radiometer. *Mon. Wea. Rev.*, **135**, 3070–3085, <https://doi.org/10.1175/MWR3454.1>.
- Ulaby, F. T., and D. G. Long, 2014: *Microwave Radar and Radiometric Remote Sensing*. University of Michigan Press, 1016 pp.
- Wang, T., C. S. Ruf, B. Block, D. S. McKague, and S. Gleason, 2018: Design and performance of a GPS constellation power monitor system for improved CYGNSS L1B calibration. *IEEE J. Sel. Top. Appl. Earth Obs. Remote Sens.*, **12**, 26–36, <https://doi.org/10.1109/JSTARS.2018.2867773>.
- Weissman, D. E., and M. A. Bourassa, 2008: Measurements of the effect of rain-induced sea surface roughness on the QuikSCAT scatterometer radar cross section. *IEEE Trans. Geosci. Remote Sens.*, **46**, 2882–2894, <https://doi.org/10.1109/TGRS.2008.2001032>.
- , —, and J. Tongue, 2002: Effects of rain-rate and wind magnitude on SeaWinds scatterometer wind speed errors. *J. Atmos. Oceanic Technol.*, **19**, 738–746, [https://doi.org/10.1175/1520-0426\(2002\)019<0738:EORRAW>2.0.CO;2](https://doi.org/10.1175/1520-0426(2002)019<0738:EORRAW>2.0.CO;2).
- Yu, T.-W., and V. M. Gerald, 2004: Evaluation of NCEP operational model forecasts of surface wind and pressure fields over the oceans. *20th Conf. on Weather Analysis and Forecasting/16th Conf. on Numerical Weather Prediction*, Seattle, WA, Amer. Meteor. Soc., P4.18, https://ams.confex.com/ams/84Annual/techprogram/paper_68792.htm.
- Zavorotny, V. U., and A. G. Voronovich, 2000: Scattering of GPS signals from the ocean with wind remote sensing application. *IEEE Trans. Geosci. Remote Sens.*, **38**, 951–964, <https://doi.org/10.1109/36.841977>.
- Zeng, X., M. Zhao, and R. E. Dickinson, 1998: Intercomparison of bulk aerodynamic algorithms for the computation of sea surface fluxes using TOGA COARE and TAO data. *J. Climate*, **11**, 2628–2644, [https://doi.org/10.1175/1520-0442\(1998\)011<2628:IOBAAF>2.0.CO;2](https://doi.org/10.1175/1520-0442(1998)011<2628:IOBAAF>2.0.CO;2).
- Zhang, H.-M., J. J. Bates, and R. W. Reynolds, 2006: Assessment of composite global sampling: Sea surface wind speed. *Geophys. Res. Lett.*, **33**, L17714, <https://doi.org/10.1029/2006GL027086>.
- Zhang, S., Z. Pu, D. J. Posselt, and R. Atlas, 2017: Impact of CYGNSS ocean surface wind speeds on numerical simulations of a hurricane in observing system simulation experiments. *J. Atmos. Oceanic Technol.*, **34**, 375–383, <https://doi.org/10.1175/JTECH-D-16-0144.1>.

IN-ORBIT PERFORMANCE OF THE CONSTELLATION OF CYGNSS HURRICANE SATELLITES

CHRISTOPHER RUF, SHAKEEL ASHARAF, RAJESWARI BALASUBRAMANIAM, SCOTT GLEASON, TIMOTHY LANG, DARREN MCKAGUE, DORINA TWIGG, AND DUANE WALISER

This document is a supplement to “In-Orbit Performance of the Constellation of CYGNSS Hurricane Satellites,” by Christopher Ruf, Shakeel Asharaf, Rajeswari Balasubramaniam, Scott Gleason, Timothy Lang, Darren McKague, Dorina Twigg, and Duane Waliser (*Bull. Amer. Meteor. Soc.*, **100**, 2009–2023) • ©2019 American Meteorological Society • Corresponding author: Prof. Christopher Ruf, cruf@umich.edu • DOI:10.1175/BAMS-D-18-0337.2

WIND SPEED RETRIEVAL UNCERTAINTY $> 20 \text{ m s}^{-1}$. A histogram of the stepped-frequency microwave radiometer (SFMR) wind speeds measured during the overpasses is shown in Fig. ES1. The maximum wind speed in the histogram is 54 m s^{-1} (120 mph, category 3).

A scatterplot with all wind speed matchups between Cyclone Global Navigation Satellite System (CYGNSS) and SFMR is shown in Fig. ES2a. A histogram of the difference between each pair of wind speeds is shown in Fig. ES2b.

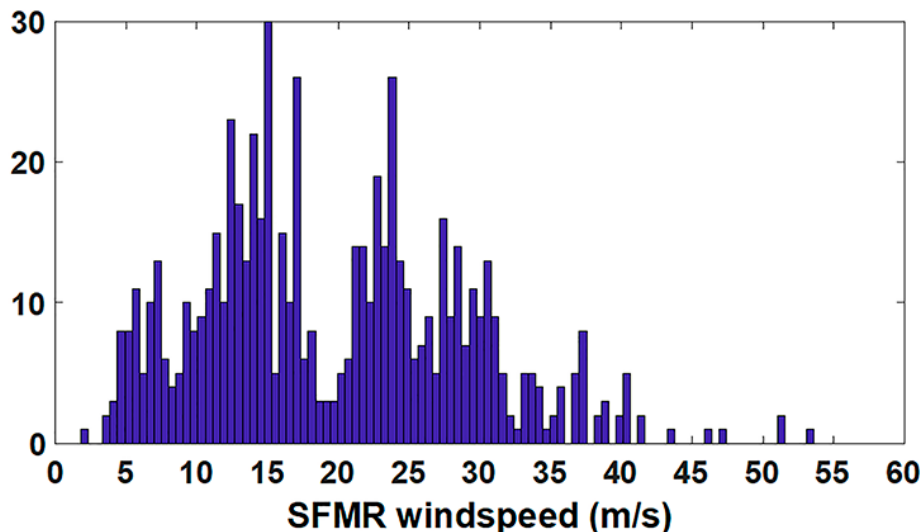


FIG. ES1. Histogram of u_{10} wind speeds measured by the SFMR on board the NOAA P-3 “hurricane hunter” aircraft during eyewall penetrations that were coincident with CYGNSS overpasses for the 2017 Atlantic hurricane season.

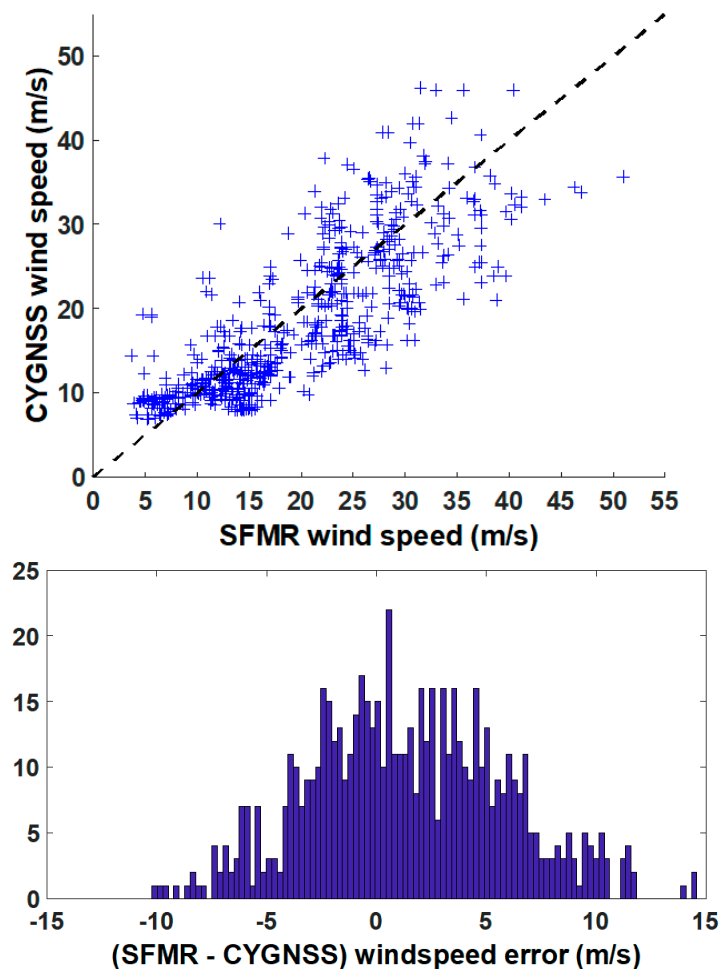


FIG. ES2. (top) Scatterplot of SFMR vs CYGNSS measurements of 10-m referenced wind speed during their coincident 2017 Atlantic hurricane overpasses and (bottom) histogram of (SFMR - CYGNSS) wind speed differences.

WIND SPEED RETRIEVAL UNCERTAINTY < 20 m s⁻¹. The buoys used for wind speed intercomparisons and performance assessments were sited throughout the tropical Atlantic, Pacific, and Indian Oceans, as shown in Fig. ES3. Also noted in the figure is the number of intercomparison samples available at each site. Histograms of wind speed measurements by CYGNSS and the full array of buoys for all intercomparison samples are shown in Fig. ES4.

SPATIAL RESOLUTION. Figure ES5 illustrates the instantaneous field of view (IFOV) as a function of incidence angle for the high- and low-altitude limits of the CYGNSS orbit. Figure ES6 illustrates how spatial resolution affects the CYGNSS mean daily coverage.

The spatial resolution of CYGNSS reflections over land is a function of the terrain. For land surfaces where large-scale topography and small-scale (with respect to the ~19-cm GPS wavelength) surface roughness is significant, the received power is distributed over a surface region analogous to an ocean rough-sea glistening zone (with varying surface facets returning power from a potentially wide area). However, in cases where the surface roughness variation (i.e., the standard deviation of surface slopes) is small with respect to the 19-cm wavelength,

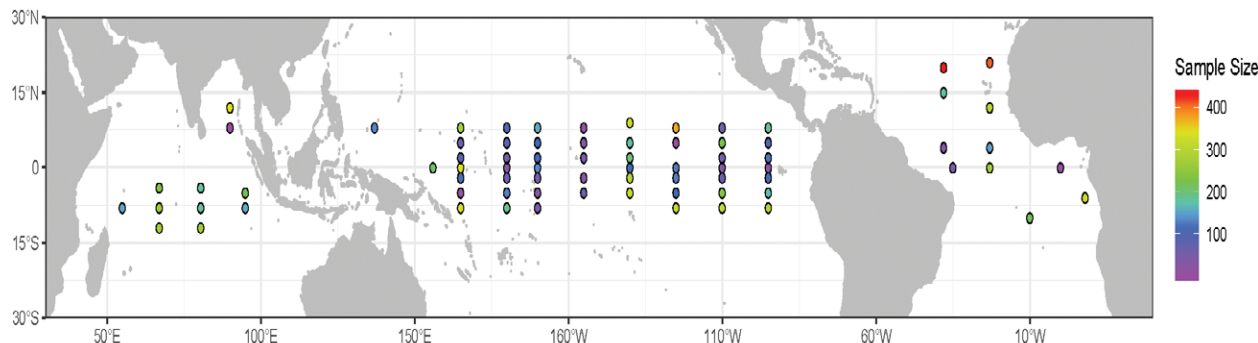


FIG. ES3. Collocated CYGNSS and buoy (18 Mar 2017–23 Aug 2018) sample size in the tropical moored-buoy array: Prediction and Research Moored Array in the Tropical Atlantic (PIRATA), Research Moored Array for African–Asian–Australian Monsoon Analysis and Prediction (RAMA), and Tropical Atmosphere Ocean (TAO)/Triangle Trans-Ocean Buoy Network (TRITON). More details on the tropical buoys are given on the NOAA/PMEL website (www.pmel.noaa.gov/gtmba/mission).

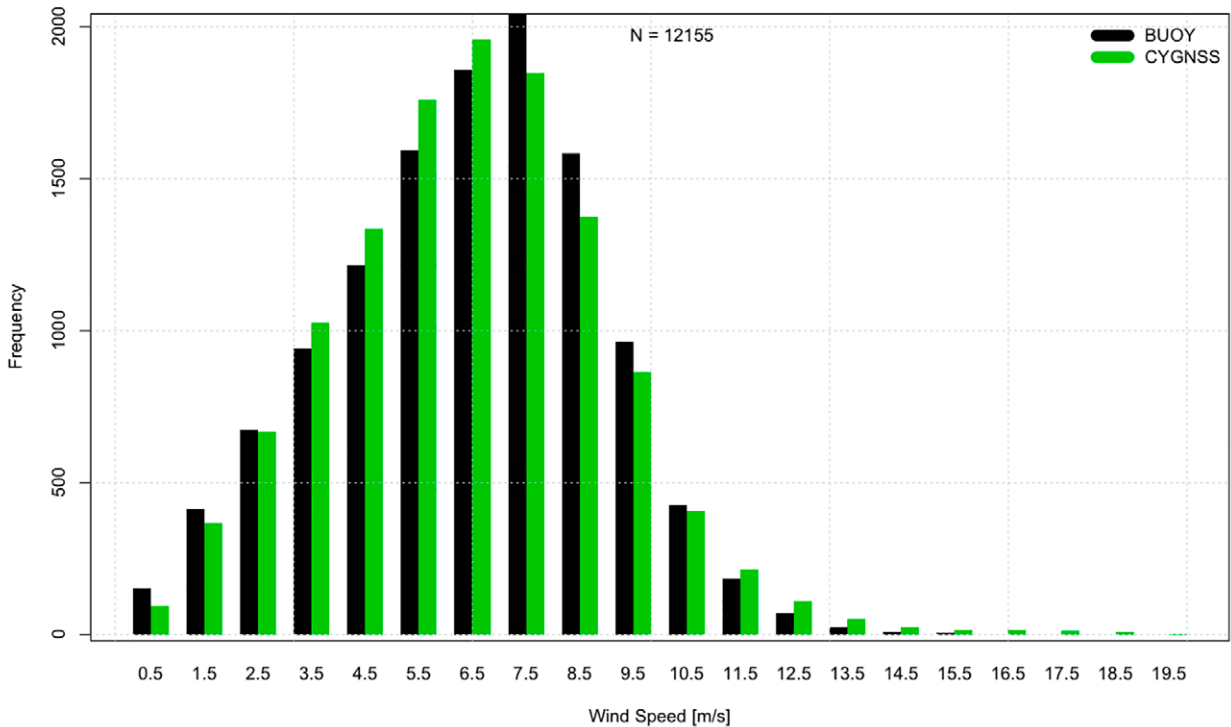


FIG. ES4. Surface wind histograms (bin width: 1 m s^{-1}) for CYGNSS and buoys.

coherent surface reflections can result. In case of a coherent surface reflection, the surface spatial area contributing to the received power in the delay Doppler map (DDM) area (DDMA) pixels will be dominated by the first Fresnel zone (where local surface propagation paths within one-quarter wavelength ($\sim 5 \text{ cm}$) will constructively interfere). The first Fresnel zone size determined by the semimajor and semiminor axes of an ellipse is a function of the reflection incidence angle. Figure ES7 shows the area and the dimensions of the two ellipse axes as a function of incidence angle. The semimajor axis will generally align with the specular point direction of travel and increases faster than the semiminor axis with incidence angle.

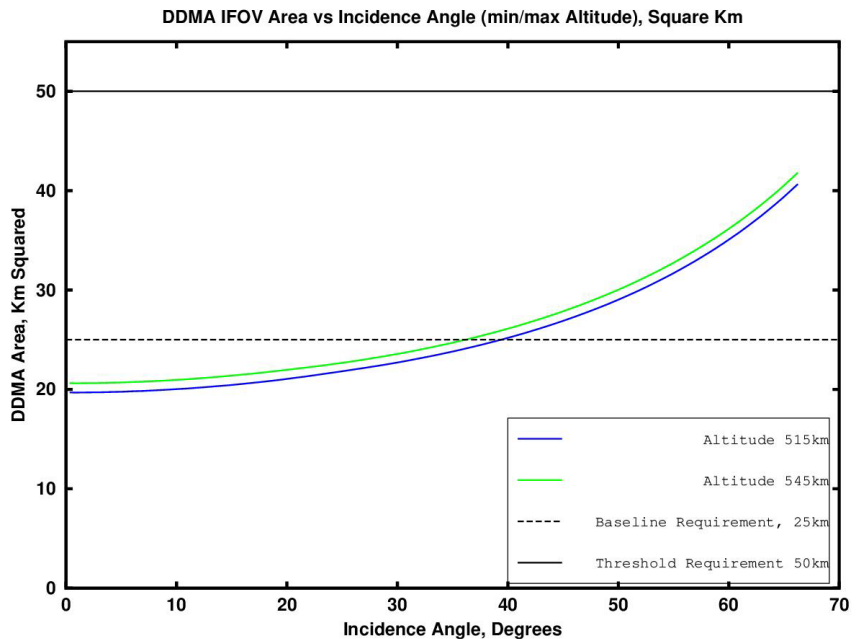


FIG. ES5. CYGNSS observation IFOV spatial resolution as a function of incidence angle for a range of observatory altitudes. The baseline requirement of 25 km met or exceeded below approximately 38° , while the threshold requirement of 50 km is always met.

A second factor determining spatial resolution (for both ocean and land measurements) is the 1-s integration performed for each DDM. This causes the first

Mean Daily Coverage vs. Specular Point Incidence Angle
 Total Valid L2 Wind Speed Samples: 409,191,159
 2017-03-18 - 2018-11-30

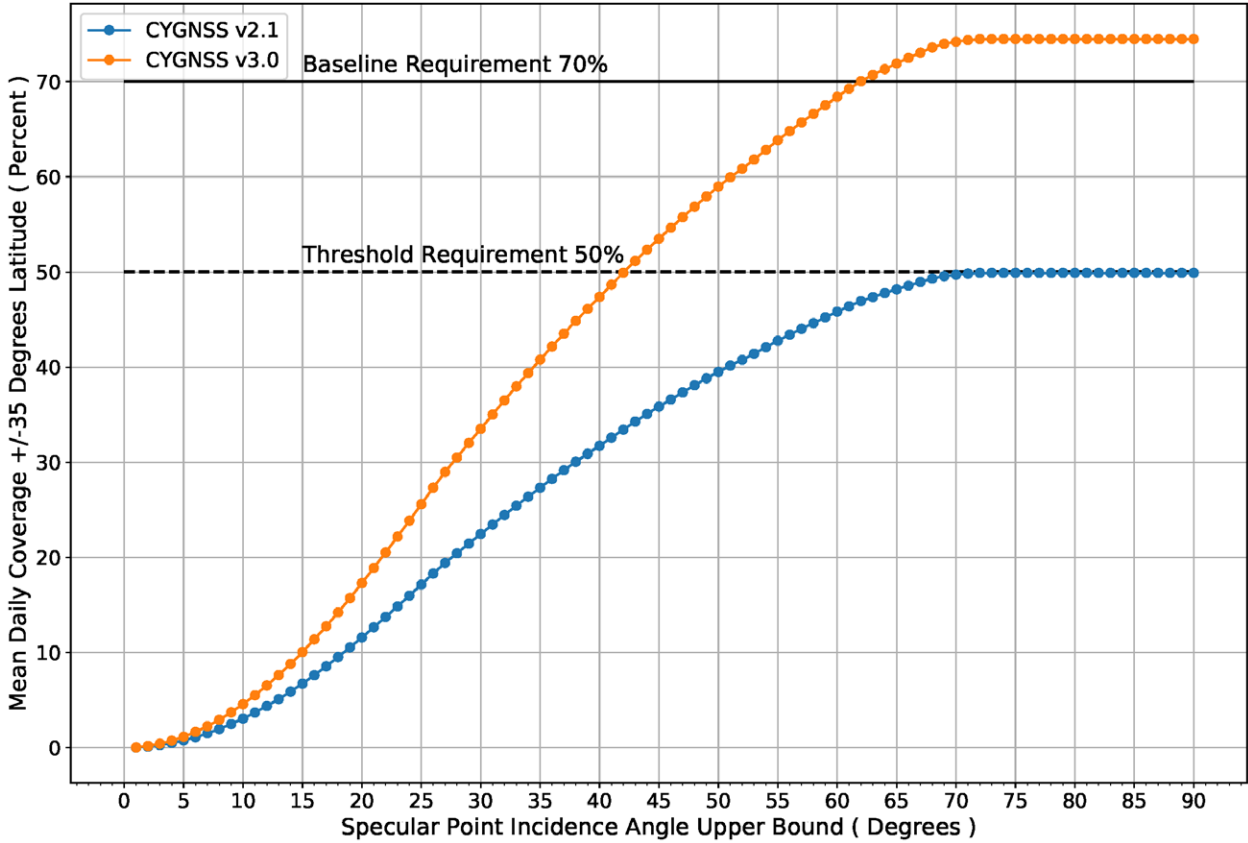
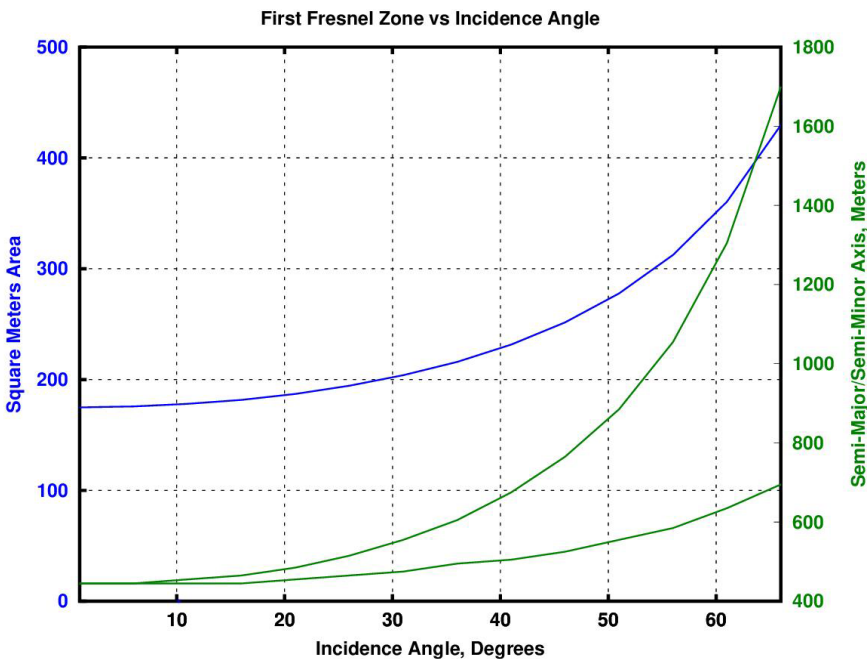


FIG. ES6. Relationship between CYGNSS mean daily coverage baseline and threshold requirements as a function of observation incidence angle for CYGNSS level I calibration, versions 2.1 and 3.0. The v3.0 calibration enables the inclusion of the GPS block type IIF satellites, which significantly increases the number of usable observations.



◀ FIG. ES7. Area of first Fresnel zone and semimajor and semiminor axes of the surface ellipse. The semimajor axis generally aligns across track to the specular point direction of travel and increases at a higher rate than the semiminor axis as a function of incidence angle.

Fresnel zone to be smeared across the surface for cases of land coherent reflection. How the 1-s integration maps to movement of the specular point across the surface is a function of the relative geometry and velocities of the CYGNSS observatory and GPS transmitter. Figure ES8 shows the distribution of specular point velocities for 10 days of measurements. The mean velocity of approximately 6 km s^{-1} results in the single-look surface area (glistening zone of Fresnel zone) being smeared over the surface on average by 6 km.

Figure ES9 shows an example of a coherent CYGNSS land reflection across a small lake

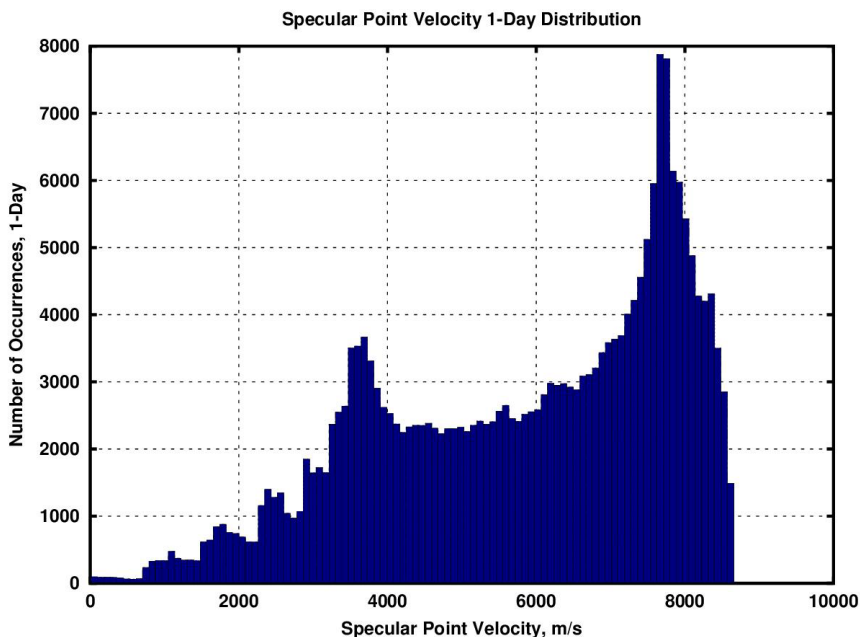


FIG. ES8. The speed of the CYGNSS specular point motion across the surface is a function of the relative observatory and GPS transmitter vector velocities and can vary between 2 and 9 km s^{-1} , with an average of approximately 6 km s^{-1} .

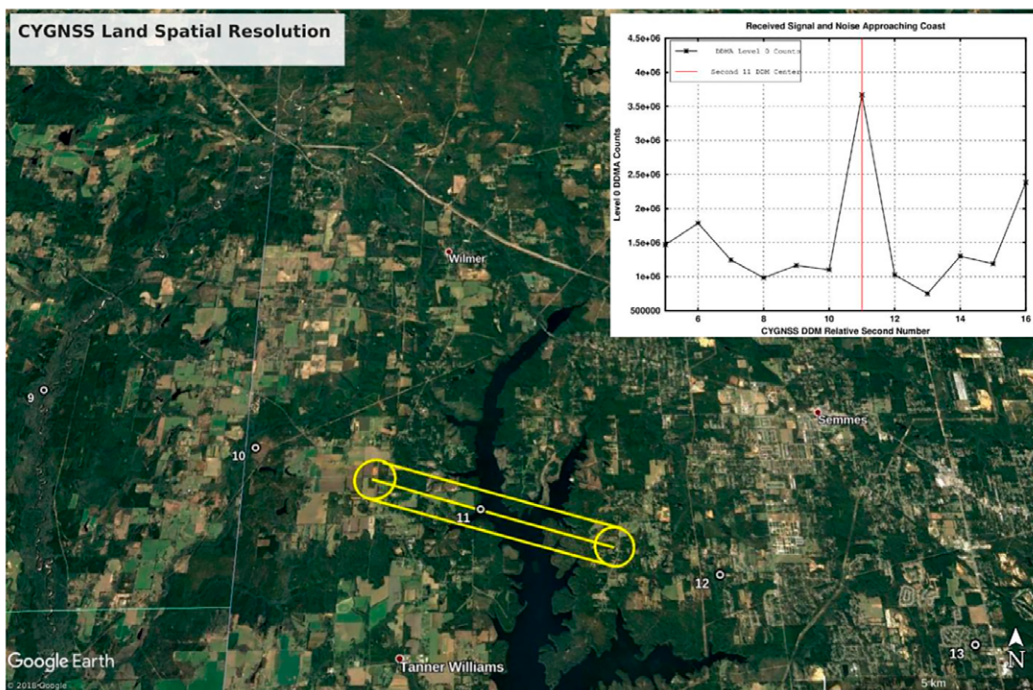


FIG. ES9. An example of an integrated Fresnel zone for a coherent specular reflection from Big Creek Lake (Mississippi). For this relatively low-incidence-angle reflection ($\sim 15^\circ$) the Fresnel zone is a $\sim 500\text{-m}$ -radius circle. The start and end 1-s integration Fresnel zones are shown as circles at the start and end of the integration. For this example, the total Fresnel spatial surface area for this measurement is $\sim 3.15 \text{ km}^2$ ($0.5 \text{ km} \times 6.3 \text{ km}$). The fluctuations in the signal level (upper-right insert) clearly show the coherent reflection from Big Creek Lake originating within the first Fresnel zone.

in Mississippi. The 1-s integration starts and ends on either side of the lake. The first Fresnel zone is shown integrated across the surface, resulting in elongated spatial resolution. The coherent reflection of the small lake (roughly 1.5 km across the observation track) is clearly visible in the increased power received. The area of the integrated Fresnel zone in this case is approximately 3.15 km² (0.5-km

Fresnel radius × 6.3-km time integration). This clearly demonstrates the potential for significantly improved spatial resolution when the conditions for coherent reflection exist.

TEMPORAL REVISIT. Figure ES10 shows a histogram of the revisit times over the life of the mission.

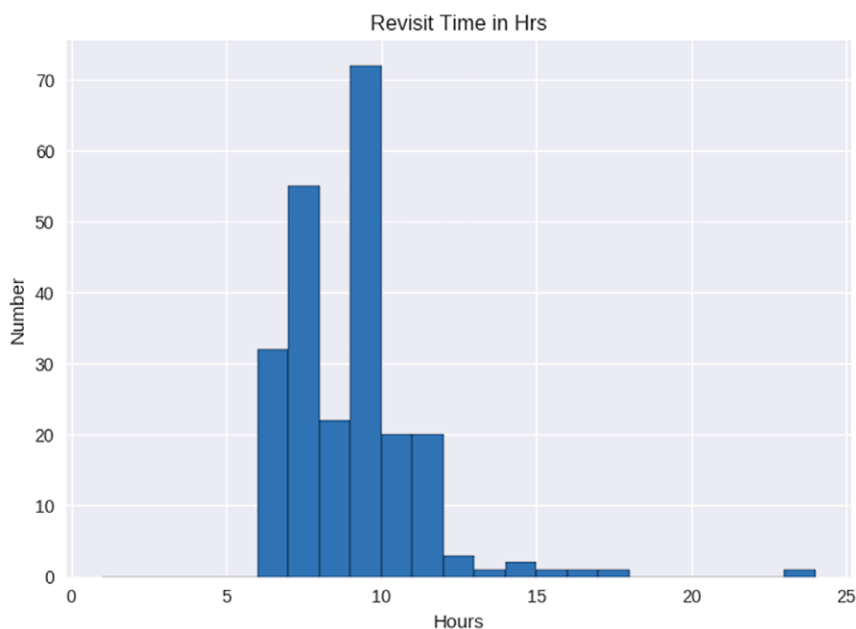


FIG. ES10. Histogram of CYGNSS L2 revisit times.